Theoretical examination of the hydroxide transport in cobaltocenium-containing polyelectrolytes

Sachith Wickramasinghe,[†] Alexandria Hoehn,[†] Shehani T. Wetthasinghe,[†] Huina Lin,[†] Qi Wang,[‡] Jacek Jakowski,[¶] Vitaly Rassolov,[†] Chuanbing Tang,[†] and Sophya Garashchuk*,[†]

†Department of Chemistry & Biochemistry, University of South Carolina, Columbia, South
Carolina 29208, United States

‡Department of Mathematics, University of South Carolina, Columbia, South Carolina 29208, United States

¶Center for Nanophase Materials Science, Oak Ridge National Laboratory, Oak Ridge,

Tennessee 37830, United States

E-mail: garashchuk@sc.edu

Abstract

Polymers incorporating the cobaltocenium groups have received attention as promising components of the anion-exchange membranes (AEM), exhibiting good balance of the chemical stability and high ionic conductivity. In this work we analyze the hydroxide diffusion in the presence of cobaltocenium cations in aqueous environment, based on the the molecular dynamics of model systems confined in one dimension to mimic the AEM channels. In order to describe the proton hopping mechanism, the forces are obtained from the electronic structure

computed at the Density Functional Tight Binding level. We find that the hydroxide diffusion depends on the channel size, modulation of the electrostatic interactions by the solvation shell and its rearrangement ability. The hydroxide diffusion proceeds via both, the vehicular and structural diffusion mechanisms with the latter playing a larger role at low diffusion coefficients. The highest diffusion coefficient is observed under the moderate water densities (around half the density of liquid water) when there is enough water molecules to form the solvation shell reducing the electrostatic interaction between ions, yet there is enough space for the water rearrangements during the proton hopping. The effects of the cobaltocenium separation, orientation, chemical modifications and the role of the nuclear quantum effects are also discussed.

1 Introduction

Ion-exchange polyelectrolyte-based membranes have a wide range of applications in energy conversion/storage devices, such as alkaline fuel cells, redox flow batteries, electrodialysis, and electrolytes. 1-3 In the case of alkaline fuel cells, free hydroxyl anions produced in the cathode are transported through an ion-exchange membrane to the anode side to participate in the oxidation reaction with fuels. 4-6 Polyelectrolytes containing the ammonium-based cations yield high hydroxide mobility, and, consequently, they are often considered as candidates for the anion exchange membranes (AEMs), ^{7–11} yet they are prone to chemical degradation under the working conditions of fuel cells. 10 Thus, the development of advanced AEMs with sufficient chemical stability and high anionic conductivity under extremely harsh and highly basic conditions in alkaline fuel cells remains an outstanding scientific challenge 4,12,13 motivating this work. Understanding the mechanisms of the hydroxide transport inside polyelectrolyte membranes, and the factors influencing this process, is highly desirable for rational design of stable and highly conductive AEMs. 7-9,14-16 The main focus of this study are the organometallic cobaltocenium-containing copolymers, which is a new class of AEMs with promising mechanical, thermal, and chemical stabilities observed under harsh conditions of the alkaline fuel cells. 1,3,10,13,17 Such membranes are made with a hydrophobic polyethylene backbone to maintain mechanical stability and hydrophilic cobaltocenium side chains to achieve rapid hydroxide transport. The morphology of the cobaltocenium polyelectrolyte membrane is characterized by the phase separation into the hydrophobic and hydrophilic domains, and the hydroxide transport occurs within the hydrophilic domains. The hydrophobic domain contains the carbon backbone of the polymer, and the hydrophilic domain contains the ionic component, including the cobaltocenium cation, water, and the hydroxyl anion (hydroxide). This phase-separated morphology restricts the hydroxide transport to a single domain. The cobaltocenium cation and the water – hydroxide system connected through hydrogen bonding network are shown in Fig. 1(a,b).

There are two mechanisms involved in the hydroxide transport – structural (Grotthuss mechanisms)¹⁸ and vehicular diffusion^{7,16} – just as it is the case for the proton (hydronium) diffusion

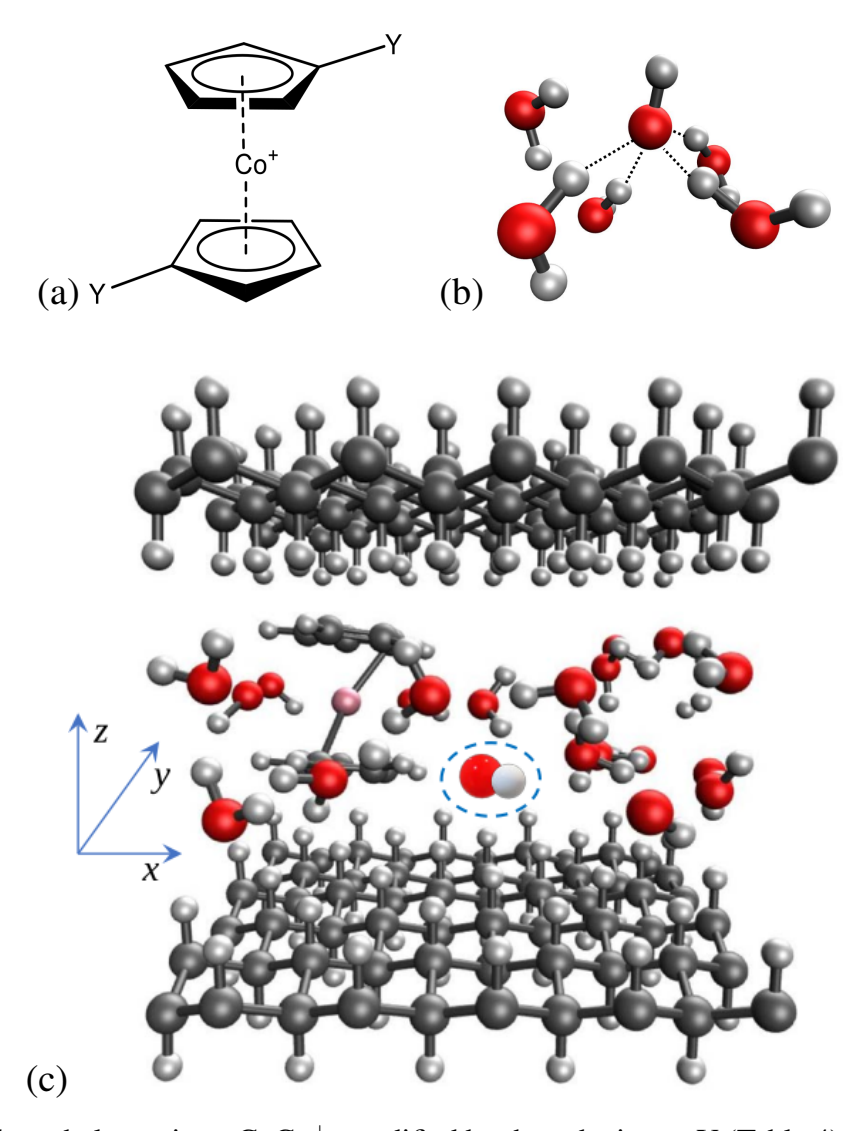


Figure 1: (a) The cobaltocenium, $CoCp_2^+$, modified by the substituent Y (Table 4) on the cyclopendadienyl ring, Cp. (b) The hydrated hydroxide complex, $OH^-(H_2O)_4$, with an additional water molecule; dashes indicate the hydrogen bonds. (c) The molecular model of OH^- diffusion in the presence of $CoCp_2^+$ ions. The size of the simulation cell is $(L_x, L_y, L_z) = (12.66, 13.36, 40.0)$ Å; the separation between the graphane layers is 10.0 Å. Carbon, oxygen, cobaltocene and hydrogen atoms are shown as grey, white, ping and red spheres, respectively. The hydroxide is circled with the dash.

under acidic conditions. In the aqueous medium, the hydroxyl ions coordinate with the water molecules, and the movement of this hydroxide-water structures is known as vehicular diffusion. In structural diffusion, a proton from the coordinated water molecules jumps (hops) to the hydroxide oxygen to form a water molecule and a new hydroxyl anion. This process is known to be faster than vehicular diffusion process. ^{3,7,19,20,20}

While the key step of the hydroxide structural diffusion is the proton transfer, the mechanisms of the structural diffusion of the protons and hydroxyl anions are noticeably different. In aqueous medium, the excess proton is part of the H₃O⁺ ion, which is coordinated by three other water molecules via hydrogen bonds to form H₃O⁺(H₂O)₃ complex. Then, the excess proton jumps to one of the coordinated water molecule forming $[H_2O \cdots H \cdots OH_2]^+$ intermediate complex. ¹⁸ A 'naive' hydroxide counterpart to this picture would involve coordination of the hydroxyl ion to three water molecules and formation of OH⁻(H₂O)₃, followed by the proton hop from one of the coordinated water molecules to hydroxide via [HO···H···OH] intermediate complex. However, the spectroscopic data and computational studies suggest that the hydroxide and proton diffusion processes are distinct:²¹ the hydroxyl ions accept four hydrogen bonds (H-bonds) from the coordinated water molecules to form an approximately planar OH-(H2O)4 structure, and in half of these complexes the hydrogen of the hydroxyl ions forms weak H-bonds with one other water molecule. Next, one of the H-bond from the planar $OH^-(H_2O)_4$ breaks to form the tetrahedral OH⁻(H₂O)₃ complex. Then, the hydrogen on the hydroxide group forms weak H-bond with another water molecule and the proton transfer results in a new OH⁻(H₂O)₃ structure. Finally, this new OH⁻(H₂O)₃ complex becomes OH⁻(H₂O)₄ complex, completing the hopping step. ^{20–23} In general, the hopping probability is higher if the hydroxide is well coordinated to the water molecules. Therefore, at low hydration the anion transport is expected to proceed mainly via vehicular diffusion and to yield low diffusion coefficients, while higher hydration levels are expected to yield higher diffusion coefficients. According to a multiscale reactive dynamics study of the hydroxide diffusion within the AEM environment, 9 the diffusion coefficient is 10 times smaller than the bulk water value due to the nature of the channels and the interactions with polymeric components. Moreover, the energy barrier is ~ 1.6 kcal/mol higher compared to the proton diffusion due to the charge localization in hydroxide, which leads to low hopping rates. Separate studies demonstrate a 10-fold change of the diffusion coefficient over the hydration range between 5.01 and 20.35 1/1000 Å 3 . 7,15,16

To provide insight into hydroxide diffusion in cobaltocenium-containing AEMs and to inform their experimental design, in this work we model diffusion at the atomistic level and investigate the effect of various factors on the hydroxide diffusion coefficients. Specifically, we study the dependence of the diffusion coefficient on the hydration level, on the cation separation and orientations, estimate the nuclear quantum effect (NQE) and explore the effect of the substituent groups on the cyclopentadienyl (Cp) rings of the cobaltocenium on the hydroxide diffusion. The remainder of the paper is organized as follows: Section 2 describes the molecular model and computational methods; the results are presented and discussed in Section 3; Section 4 concludes.

2 Methods

The molecular model. Typical computational studies of AEMs that capture their morphology and hydration of a polymer involve molecular dynamics (MD) of several thousand atoms. ^{14,24–27} For practical reasons, such simulations typically employ force fields to describe the interactions between atoms. However, most force fields do not describe processes involving bond breaking and reforming. Given the focus of our current studies on the structural diffusion of OH⁻ which involves bond-breaking/reforming, and the presence of cobaltocenium cations (force fields typically do not have parametrization for Co atoms), we have employed ab initio molecular dynamics based on the Density Functional Tight Binding (DFTB). ^{28,29} The DFTB is a semi-empirical electronic structure method, which allows for a quantum chemical description of bond breaking and reforming and is practical for dynamics on the 100-picosecond time scale for molecular system consisting of a several hundred atoms. ^{30,31}

To limit the molecular model size for practical reasons, we use a simplified atomistic represen-

tation of the AEM that follows the ab initio MD studies of the hydroxide diffusion in quaternary ammonium-based AEMs. ^{7,16} In our model of AEM the hydrophilic environment confined by the hydrophobic polymer backbones is represented as a domain between two graphane sheets and consists of total over 500 atoms. The confinement eliminates configurational randomness of the polymer segments of the full atomistic description, ²⁷ yet the model remains adequate to study the mechanisms of the OH⁻ transport and its dependence on such parameters of a system as the cation spacing, water density, temperature, cobaltocenium orientation and substitutions.

The simulation cell. To realistically describe properties of extended AEM system, a periodic boundary condition were employed with large orthorhombic unit cell of size $L_x \times L_y \times L_z$ and L_z =40 Å. A representative simulation cell is shown in Fig. 1(c). The unit cell consists of two hydrophobic graphane sheets parallel to the xy-plane and separated by 10 Å in the z-direction, followed by 30 Å of vacuum. The cell size – approximately the same in x and y directions – corresponds to the cation separation. The periodic boundary conditions provide continuity of the hydrophilic domain. Each cell contains one $Co(Cp)_2$ cation with Co centered between the graphane layers and one OH^- . The molecular model is completed by 10 to 40 water molecules representing different hydration levels. This range corresponds to the number density varying from 7.9 to 31.7 molecules per 1000 ų, or from 23.7% to 95% of the bulk water density. To explore the effects of the cation spacing several cell sizes have been considered: the cell size L_y was kept constant at 13.36 Å, and the L_x was varied from about 12 to 22 Å. The exact values of L_x were adjusted to match the periodicity of the graphane sheets. The nuclei of the graphane sheets and of the cation are kept frozen during MD.

The effect of the water density and cation spacing is analyzed from MD of the model with unsubstituted $CoCp_2^+$, whose carbon rings are kept parallel (zero angle) to the graphane sheets. The effect of $CoCp_2^+$ orientation is probed by comparing MD with the carbon rings fixed at 0, 45° and 90° relative to the graphane sheets. The effect of Cp modifications is examined by performing MD of $CoCp_2^+$ with one of the hydrogen atoms in each Cp replaced by substituent groups pointing

in the opposite directions. For the orientation and substituent studies the cell size is $L_x = 12.66$ Å and $L_y = 13.36$ Å with the cell contains 20 water molecules, which corresponds to 'moderate' water density of about 50% of the bulk water. Given our focus on the hydroxide transport, in all simulations the list of atoms which are allowed to move freely is limited to those of water and hydroxide, which eliminates degradation of $CoCp_2^+$ and deprotonation of the graphane sheets from the model.

The energy and forces evaluation. The potential energy and intermolecualr forces in this study are computed using 2nd order Seslf Consisted Charges (SCC) DFTB and with periodic boundary conditions and Gamma point sampling. While popular parameterized force fields provide the most practical option for MD of large systems, they are inadequate to study the structural diffusion ^{32,33} mechanism in which covalent O–H are constantly created and broken. More sophisticated force fields have been developed to allow for the proton transfer between H₃O+ and H₂O, but as shown in Refs ^{11,34} such force fields are not sufficiently accurate for the proton hopping between H₂O and OH⁻. The force fields developed to describe the structural diffusion of H₃O+ and of OH⁻ include sOSS2 potential for bulk water, ³⁵ and ReaxFF with CHNO-2017_weak for the hydroxide diffusion in quaternary ammonia-based AEM. ^{14,27,33} At the time of this study, the ReaxFF parametrization has not yet been extended to the transition metals. Thus, with the full DFT based *ab initio* MD simulations being impractical for our system composition, size and time-scales, we have chosen the semi-empirical DFTB method ^{28,29} as a compromise between the accuracy and numerical cost of on-the-fly MD.

DFTB is an approximate DFT method based on tight-binding Slater-Koster model for valence electrons with core electrons neglected. The effect of core electron on overall energy and forces is included, along with the internuclear repulsion, through two-center repulsion potentials. The pre-calculated Slater-Koster coefficients and repulsion potentials are transferable and stored in a tabulated distance-dependent format in parameter files akin to pseudopotentials. The electron repulsion term for valence electrons is included self-consistently via self-consistent charge equi-

libration algorithm.^{36,37} The computational cost of DFTB is about 100 to 1000 times lower than of the conventional DFT methods and allows routine MD simulation of 1000+ atoms molecular systems with periodic boundary condition on the 100 ps timescale.^{37,38}

The DFTB has been successfully used to study the hydroxide diffusion and proton diffusion in bulk water. ^{39,40} The proton diffusion coefficients calculated with DFTB are equal to 0.90 Å²/ps, and agree very well with the experimental value of 0.94 Å²/ps. ⁴⁰ For the hydroxide diffusion the agreement not as good but still acceptable – ranging between 0.53 Å²/ps and 0.67 Å²/ps depending on specific algorithm used. As a note of caution, unphysical pockets of voids with no or very little water density during the SCC-DFTB MD simulations were reported in Ref. ⁴¹ In this work, we use SCC-DFTB with periodic boundary condition and Gamma point sampling as implemented in DFTB+ package ⁴² with *trans* and *mio* parameters, ⁴³ and with the Fermi-Dirac smearing at electronic temperature equal to 300 K.

The MD simulation. The estimated diffusion coefficients and mechanism are obtained from the evolution of a microcanonical NVE ensemble (the number of particles, N, volume, V, and energy, E, are constant) with the energy being set to the equivalent of 300 K. To reach the target temperature, T, the system is equilibrated for about 5 ps as an NVT (constant N, V and T) ensemble by coupling to the Nose-Hoover thermostat prior to NVE simulations. ⁴⁴ To assess the thermalization level, the fluctuations of the kinetic energy and its average are compared to k_BT over the last 1 ps of the NVT trajectories. (For a system in thermal equilibrium the ratio of the kinetic energy fluctuations to the mean kinetic energy should approach $1/\sqrt{3N_{at}}$, where N_{at} is the number of the moving atoms). The system configurations from the equilibrated part of the NVT run are used to initiate the NVE dynamics. As mentioned above, the nuclei of $CoCp_2^+$ and graphane sheets were frozen during the simulations. The analysis is based on the dynamics of the ensemble of 20-25 trajectories, referred to as 'replicas', representing the same test system. The initial positions for each replica are the snapshots sampled from the equilibrated part of the computed NVT trajectory, and the initial momenta corresponding to 300 K are randomly generated. Then the trajectory

undergoes additional 5 ps NVT equilibration, followed by the NVE dynamics of 10 ps. The propagation time-step is set to 1 fs yielding the energy conservation over 10 ps of better than 1%. The trajectory data for the analysis are recorded every 10 fs. The diffusion coefficients are computed for each replica and averaged over the replicas. For each type of system the cumulative NVE dynamics time adds up to at least 200 ps. The main computational cost is 25×10^4 electronic structure calculations during the NVE run. The workflow is summarized in Table 1.

Table 1: The workflow for the MD simulations using $N_r=25$ replicas instead of a single trajectory. The number of particles, N ≈ 500 , is constant throughout; the simulation temperature is T=300 K; the time step is 1 fs.

Task	Details and comments	Cost
	take xyz coordinates from the existing structure files	
Initialize NVT	for the optimized graphane sheets and cobaltocenium	
	H ₂ O (10 to 40 molecules) and OH ⁻ are movable	
NVT run	thermalize H ₂ O and OH ⁻ using Nose-Hoover	2×10^4 steps
	thermostat is at 300 K; every 10th frame is saved	2×10^3 frames
NVT check	equilibration error is computed from the frames [1900, 2000]	
	thermalization is typically achieved after 1000 frames	
	define replicas as:	
Initialize NVE	xyz from the thermalized part (frames [1000, 2000]) of NVT	25 replicas
	random velocities corresponding to 300 K for movable atoms	
short NVT	equilibrate the active DOFs for each replica	5×10^3 steps
NVE run	the main MD part: propagate all replicas in parallel	$N_r \times 10^4$ steps
Analysis	export the trajectory data: positions, velocities and charges	10^3 frames
	analyze trajectory data outside DFTB+ using python scripts	per replica

Taking advantage of ergodicity of classical dynamics with conservative forces, i.e. of the fact that the information in a single long trajectory approaches that of multiple short trajectories in the infinite time limit, we use replicas, rather then a single long trajectory of comparable total length, for the following reasons. Firstly, since the forces acting on the trajectories come from self-consistent electronic structure method, maintaining constant energy during long NVE trajectory requires very tight convergence of the forces, which significantly increases the simulation cost. For a system with 20 moving water molecules propagated at 300K with 1 fs time-step, the energy variation over 50 ps is 1.2%, while it grows to 11% for the 300 ps propagation. Secondly, the proton hops during the hydroxide diffusion are rather rare (about 0.1 hops per ps), and randomization of

the initial momenta defining the replicas provides more accurate representation of the system. A comparison of the diffusion coefficient obtained from 10 and 50 ps replicas is given in Fig. S1. Finally, running shorter trajectories in parallel affords more interactive analysis and is simply more practical.

The MD analysis. The key property of interest here is the diffusion coefficient, D, which for a single particle, positioned at \vec{r} in n_d C-dimensional Cartesian space, is defined in terms of the mean square displacement (MSD) at the infinite time limit, 45,46

$$MSD(t) = (\vec{r}(t) - \vec{r}(0))^2, \quad D = \lim_{t \to \infty} \frac{MSD}{2n_d t}.$$
 (1)

Since our analysis is based on the dynamics of N_r replicas rather from a single long trajectory, the diffusion coefficient is averaged over them,

$$\bar{D} = \frac{1}{N_r} \sum_{n=1}^{N_r} D^{(n)}.$$
 (2)

Its standard deviation, σ_D ,

$$\sigma_D = \frac{1}{\sqrt{N_r}} \left(\sum_{n=1}^{N_r} (D^{(n)} - \bar{D})^2 \right)^{1/2}, \tag{3}$$

is interpreted as a measure of convergence of the diffusion coefficient with respect to time. In our system the hydroxide diffusion in z-direction is restricted by the hydrophobic graphane sheets. Therefore, the diffusion coefficient is computed in two dimensions ($n_d = 2$) from the displacement in x- and y-directions. To analyze the effects of the cation orientation and separation, the one-dimensional diffusion coefficients, D_x and D_y , are computed using $n_d = 1$ in Eq. (1).

A time-lag definition of the MSD. Implementation of Eq. (1) implies extrapolation of the D-value from the finite-time trajectory to the infinite time limit, which is often ambiguous. Thus, we use an alternative time-lag evaluation of D. ^{45–47} In this method the MSD is computed as a function

of the time-lag, τ , rather than of the propagation time, t:

$$MSD(\tau, \delta) = \frac{1}{n_{\tau}} \sum_{j=0}^{n_{\tau}} \left(\frac{1}{N_r} \sum_{n=1}^{N_r} \left(r^{(n)} (j\delta + \tau) - r^{(n)} (j\delta) \right)^2 \right). \tag{4}$$

where n_{τ} is the number of time lags of given duration τ and δ is the gap between two consecutive time origins. The MSD of Eq. (4) formally depends on the choice of the gap between two successive time origins, δ . According to the analysis of Ref.⁴⁵ to eliminate this dependence and avoid the sampling overlap, δ should no lesss than τ . Thus, we compute the diffusion coefficient setting $\delta = \tau$ in the MSD of Eq. (4), which is then used in Eq. (1) with $t = \tau$.

Defining the maximum time lag. To determine a reasonable value of the maximum time lag, τ_{max} (a counterpart to t_{max} for a finite time trajectory), we performed a MD simulation for 74 water molecules confined between two graphane sheets separated by a distance of 10 Å in the z-direction. The size of the simulation box in x and y is 22.78 by 13.31 Å yielding the water density close to that of bulk water. To investigate the diffusive behavior of the system, the MSD was computed for a subset of 24 randomly selected water molecules, and D was determined for different values of the maximum time-lag, τ_{max} . The resulting D as a function of τ_{max} , shown in in Fig. 2, flattens at about 1 ps. This value, $\tau_{max} = 1$ ps, is used for cobaltocenium-containing systems. Increase in τ_{max} did not significantly affect the diffusion coefficient. While we observe some minor variations for the time-lag values beyond 1 ps, these were within the statistical error. For the reference CoCp_2^+ system at the average hydration of 15.9 molecules per 1000 ų, the average diffusion coefficient derived from five 50 picosecond replicas is equal to 0.42 Ų/ps, which differs from the value derived from 25 10 picosecond replicas by 5% (Fig. SI1). We also note, that adequate representation of local structures from 1-2 ps trajectories has been recently demonstrated in the context of nonadiabatic molecular dynamics in metal halide perovskites.

Keeping track of the hydroxide. Because of the proton hopping, the hydroxide changes identity with time. Thus, throughout the simulation the hydroxide assignment is performed as follows: each hydrogen is assigned to the closest oxygen atom; oxygen with a single hydrogen (proton)

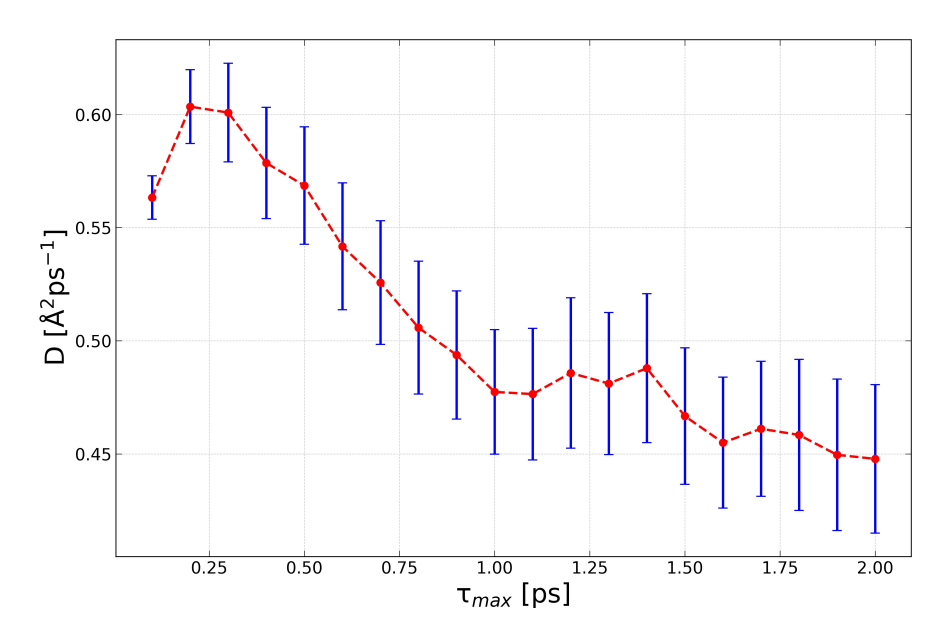


Figure 2: The diffusion coefficient for bulk water obtained from Eq. (4) as a function of the maximum time-lag, τ_{max} .

is the hydroxyl ion, whose position and the oxygen label are tracked over time. The observed back-and-forth proton exchange between the hydroxide group and its coordinated water molecule, known as rattling, is removed from the analysis, since it does not contribute to the diffusion.^{7,19} The behavior is treated as 'rattling' if the identity of the hydroxide oxygen returns to its original label within 50 fs.

Convergence test. Let us quantify the convergence of the hydroxide diffusion, D, with respect to the number of replicas for a representative reference system, i. e. the unsubstituted $CoCp_2^+$ and OH^- in a simulation cell of $12.66 \times 13.36 \text{ Å}^2$ hydrated with 20 water molecules. The analysis of the reference system is based on the dynamics of $N_r = 25$ replicas with the cumulative MD time of 200 ps. As seen in Fig. 3, D converges with the number of replicas to $\approx 0.42 \text{ Å}^2/\text{ps}$, and the statistical error σ_D over the replicas reduces to $0.060 \text{ Å}^2/\text{ps}$ or 15%.

3 Results and discussion

Unless noted otherwise, the results are obtained for the unit cell of $12.26 \times 13.36 \times 40 \text{ Å}^3$ in the xy-plane with the hydrophilic environment extending in xy direction and confined by the hydrophobic

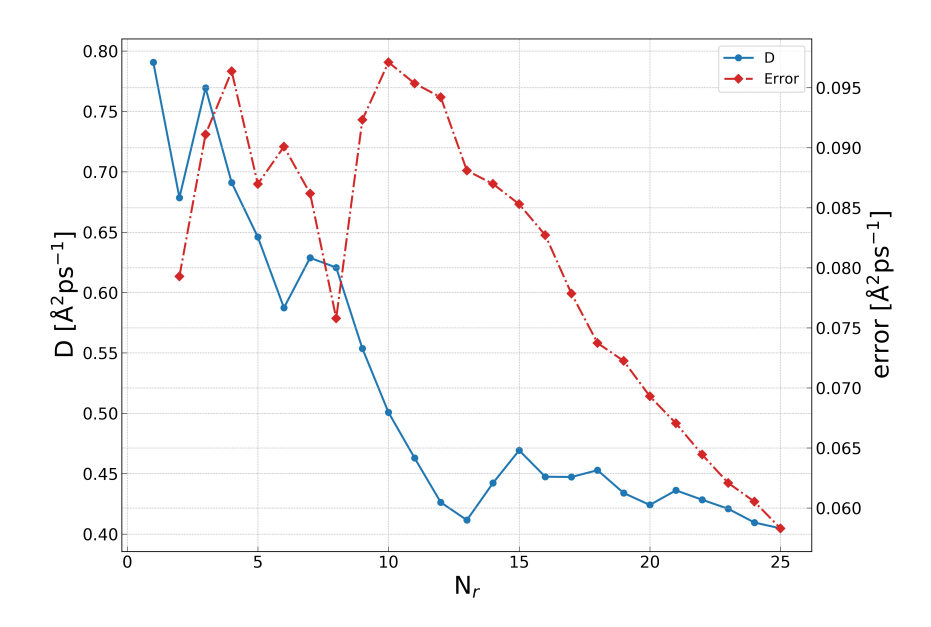


Figure 3: Convergence of the diffusion coefficient and its error with the number of replicas, N_r , for the $\text{CoCp}_2^+\text{OH}^-$ system in a cell of $12.66 \times 13.36 \text{ Å}^2$ hydrated by 30 water molecules.

polymer backbones approximated by graphane sheets separated by 10 Å. The 30 Å, vacuum separation in z-direction was added to minimize the effect of interaction of EAM with its periodic image in z-direction. The diffusion coefficients are computed in two dimensions (x and y), and 'diffusion coefficient' or D refers to that of the hydroxide.

3.1 Effect of the water density

The results of the simulations at different water densities, known to strongly affect the dominant mechanism and the coefficient of hydroxide diffusion, 49,50 summarized in Table 2 and visualized in Fig. 4, exhibit a significant non-monotonous dependence of the diffusion coefficient on the water density. As seen in Fig. 4(a), for the cell size and geometry of the reference system, the variation of the water density from 25% to 100% of the bulk value leads to a threefold change in the hydroxide diffusion coefficient, D_{OH} . Both, the lowest and the highest water densities exhibit low D_{OH} compared to those at the intermediate hydration level; the highest diffusion coefficient of 0.66 Å²/ps is seen at around 60% of the bulk water density. The dependence on the water density correlates with the diffusion coefficient computed without the hops, D'_{OH} , and with the average

number of hops, the latter given per 1 ps in Fig. 4 (vertical axis on the right-hand side).

To rationalize this trend, let us compare the hydroxide diffusion to that of all oxygen atoms, i.e. from the water and hydroxide molecules, within the same simulation. The oxygen diffusion coefficient, D_O , listed in Table 2, monotonically decreases from 1.061 to 0.075 Å²/ps with the increase of the water density. At low hydration levels the hydroxide and oxygen diffusion coefficients behave differently: under such conditions the water molecules are nearly free and move without the intermolecular collisions, while for the hydroxyl ion there is not enough water molecules for a well-formed solvation shell around the hydroxide. A complete solvation shell would screen and delocalize the negative charge of the hydroxyl ion. In its absence, however, the negative charge remains localized on the hydroxide resulting in a stronger electrostatic attraction to the cobaltocenium cation. Thus, at low hydration level stronger (compared to higher hydration level) binding limits the anion diffusion. Moreover, the incomplete solvation shell implies lack of the hydrogen bonding network necessary for the hopping. The number of hops is reduced along with the diffusion coefficient (Fig. 4). Thus, at the lowest hydration level both factors – the system energy and configuration – contribute to low hydroxide diffusion.

Table 2: The diffusion coefficients (given in Å²/ps) for the hydroxide, hydroxide with the hops excluded from the MSD, and for all oxygen atoms (including the hydroxide oxygen), denoted as D_{OH} , D'_{OH} and D_O , respectively. The water density, ρ , is listed as the number of molecules per 1000 Å^3 .

ρ	D_{OH}	D'_{OH}	D_{OH}/D'_{OH}	D_O	D_{OH}/D_{O}
7.9	0.24	0.12	1.94	1.06	0.22
15.9	0.40	0.24	1.67	0.86	0.47
19.8	0.66	0.40	1.65	0.72	0.92
23.8	0.45	0.33	1.37	0.48	0.93
31.7	0.22	0.07	3.04	0.07	2.87

In the simulations at the highest hydration level, the water molecules arrange themselves into two layers parallel to the graphane sheets, effectively reducing the domain size and increasing confinement. Consequently, the mobility of all water molecules is hindered, which leads to a reduction of the diffusion rates for both water and hydroxide species. An additional consideration for the hydroxide is that the resulting water structure hinders rearrangements of the water molecules

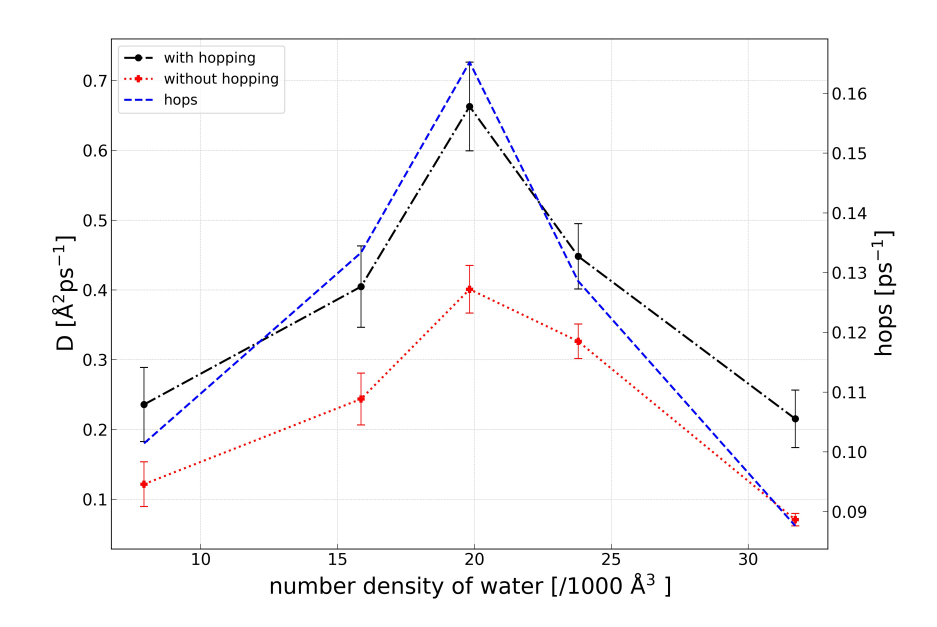


Figure 4: The hydroxide diffusion coefficient with and without hopping and the average number of hopping events under different hydration levels.

crucial for the hopping process, thus the frequency of the hopping events in this regime is reduced.

The last point is consistent with the analysis of the optimal distances between water molecules and hydroxyl ions for the occurrence of hopping events. Specifically, we measured the distance, R, between the oxygen atoms of the hydroxyl ion and its closest water molecule and tracked the identity of the hydroxide oxygen atom after 10 femtosecond interval. A change in the identity of the hydroxide oxygen atom is a marker of a hopping event. The hopping probability was estimated by analyzing various distance ranges for all five hydration levels. This involved defining specific distance ranges and then assessing the probability of finding an oxygen atom within the given distance range, along with the corresponding hopping probability while taking into account the effect of rattling. According to this analysis, smaller distances R correspond to higher hopping probabilities, with a probability exceeding 15% for R < 2.45 Å. Conversely, the probability drops below 0.5% for R > 2.55 Å. Furthermore, we have observed that for a given R-range, the hopping probability decreases as water density increases, highlighting the impact of the impeded rearrangement ability at higher densities reducing the frequency of hopping events. This trend is explained by the fact that at the highest densities, even though there are oxygen atoms close to the hydroxide, the hopping event is less likely to occur because the spatial rearrangement of the water

molecules is hindered. In contrast, at low water densities, rearrangements are easier, resulting in an increased hopping probability. However, it should be noted that low water densities may not have the highest overall hopping probability simply due to the lack of water molecules in close proximity. Nonetheless, our findings demonstrate that low water densities exhibit a higher probability of hopping when the hydroxide is in close proximity to water molecules compared to higher densities. This underscores the importance of the ability to rearrange in facilitating hopping events.

3.2 Effect of the cation arrangement

The cation spacing effect was probed by comparing MD results for the simulation cell sizes of 12.66, 17.69 and 22.75 Å in x-direction. Due to the numerical cost of the increased number of atoms, only x- direction was changed compared to the reference system. The results are summarized in Fig. 5.

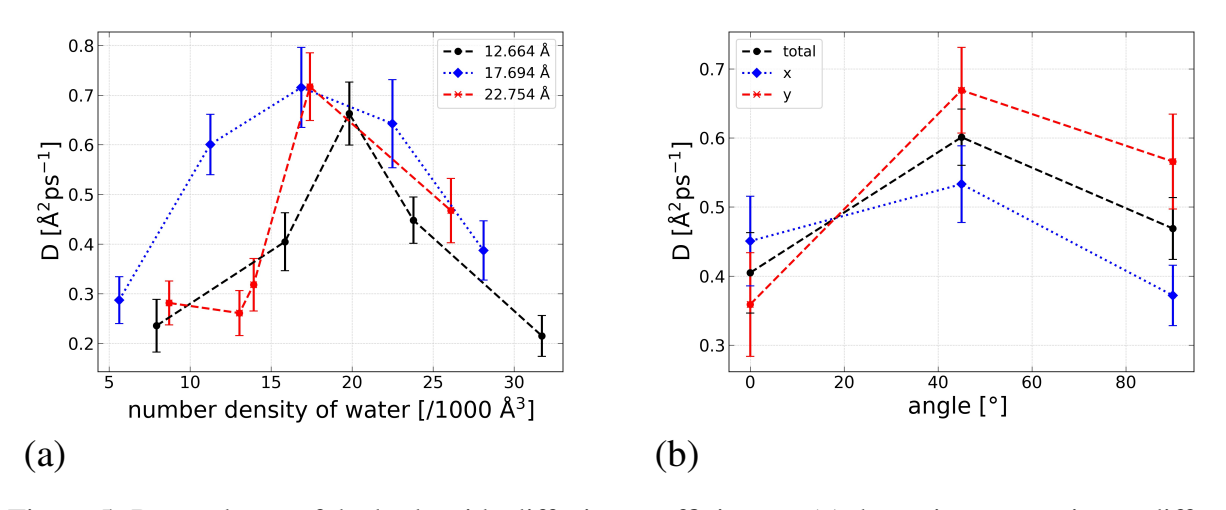


Figure 5: Dependence of the hydroxide diffusion coefficient on (a) the cation separation at different hydration levels, and (b) on the cation orientation at 15.9 $[1/1000 \text{ Å}^3]$ hydration level.

The solvated hydroxyl ion has a larger radius than the single anion, which leads to increased resistance to the vehicular diffusion from the stationary polymeric components. However, by increasing the spacing between cations the rate of the hydroxide diffusion is enhanced at a given hydration level, while the hopping contribution remains unaffected. This is due to the larger spacing between cations, which provides more space for the solvated hydroxide to diffuse via the vehicular

mechanism, resulting in a higher diffusion coefficient in larger cells within a given hydration level. A recent machine learning investigation of the quaternary and piperidine ammonium species, predicting the ionic conductivity of AEMs based on the experimental data, states that increasing the cation separation enhances hydroxide conductivity. Our results for the cobaltocenium-containing model systems derived from MD at several water densities (Fig. 5), show increase of D_{OH} with the cation separation at low to moderate water density, with the maximum diffusion coefficient of $\sim 0.7 \text{ Å}^2/\text{ps}$ attained at the number density of water of 17 [1/1000 ų] for the two larger cells. At higher water densities D_{OH} decreases for all three cell sizes.

To assess the orientation effect, the cobaltocenium has been placed at zero, 45- and 90-degree angles measured between the plane of the carbon rings on the cation and the graphane sheets; the zero degree and 90-degree angles correspond to the Cp rings being in xy- and xz- planes, respectively (Fig. 1(c)). Given the comparable diameter and spacing of the carbon rings, the orientation of the carbon ring has little effect on the channel size. Yet, as seen in Fig 5(b), there is a noticeable dependence of D on the orientation. We found that orientation had a greater influence on the diffusion coefficient in the y-direction than in the x-direction. The orientation of the Cp ring influences the electrostatic attractions between hydroxide and cobaltocenium cations, resulting in an asymmetric potential energy surface in both x- and y-dimensions. This change in the potential energy surface affects D.

Finally, for comparison with the more traditional AEM components and to probe the effect of the cation arrangement, we will briefly depart from the cobaltocenium cations and consider the hydroxide diffusion of the quaternary ammonium-based cations within the same simulation setup and protocol (Table 1). Based on recent work on AEMs characterized by the efficient ionic conductivity, alkaline resistance, chemical stability, and longevity, $^{52-55}$ we have considered the hydroxide diffusion with pyridinium, tetra-methyl ammonium (TMA), 6-azoniaspiro[5,5]undecane (ASU), and 1-ethyl pyridinium. Based on the bond dissociation energy (BDE) of the cation-hydroxide dissociation channel, estimated at the B3LYP/6-31+G** in PCM, the pyridinium (BDE \approx 37 kJ/mol) is expected to be more stable than the remaining species (BDE of \approx 13, 11 and 8 kJ/mol, respec-

tively). The MD was performed for two hydroxyl anions and two cations per single cell. The cations were separated by 10 Å in x-coordinate, and the cell of 20.22×13.36 Å² was hydrated by 32 water molecules yielding a moderate number density of water of ~ 16 [1/1000 Å³]. The cations were taken either identical (the dual cation models) or paired as pyridinium/TMA and 1-ethyl pyridinium/ASU (the double cation models). In the double cation models, the identity of OH⁻ nearest to a particular cation was tracked and the cation-specific coefficients were computed. The results are summarized in Table 3.

Table 3: Hydroxide diffusion per OH⁻ for the quaternary-ammonium or pyridinium cation pairs. The diffusion coefficient, D_{OH} , and its standard deviation, σ_D , are computed over 25 replicas. The $\sigma_D^{relative}$ is defined as σ_D/D_{OH} in percent. For the dual cation systems, D is averaged over the two hydroxyl ions.

property	pyridinium	TMA	ASU	1-ethyl pyridinium	
dual cation models					
$D_{OH} [\text{Å}^2/\text{ps}]$	0.112	0.622	0.532	0.551	
σ_D [Å $^2/\mathrm{ps}$]	0.0274	0.0425	0.0327	0.0386	
$\sigma_D^{relative}$	24.0%	6.8%	6.2%	7.00%	
double cation models					
$D_{OH} [\text{Å}^2/\text{ps}]$	0.00626	0.656	0.583	0.469	
σ_D [Å $^2/\mathrm{ps}$]	0.00119	0.0608	0.0351	0.0522	
$\sigma_D^{relative}$	19.0%	9.3%	5.6%	11.0%	

 D_{OH} from the dynamics with the identical quaternary-ammonium cations ranges from 0.112 to 0.623 Å²/ps, while the cobaltocenium value for the comparable cell size and hydration level (Table 2) is 0.40 Å²/ps. Thus, cobaltocenium is, indeed, a competitive AEM component in this respect. When considering the cation pairs, our main observation is that upon pairing of TMA and ASU with the pyridinium cations, D_{OH} associated with the pyridinium cations increases and D_{OH} associated with the non-pyridinium cations decreases. While the total diffusion coefficients of the double and the corresponding dual cation systems are nearly the same and the simulation is limited in many respects (frozen cation nuclei, cell size, hydration level, ...), the results suggest that the identity of the cation pairs may affect the diffusion and, therefore, can be used as an additional means of balancing the ionic conductivity with other desirable AEM properties such as the alkaline stability, something that we intend to explore theoretically and experimentally in the

future.

3.3 The effect of the substituent groups

Now we turn to the effect of chemical modification of the cobaltocenium cations on the hydroxide diffusion coefficient, replacing one hydrogen atom on each carbon ring with one of 12 substituent groups, Y (the same on both rings): $Y = \{CH_3, N(CH_3)_2, OCH_3, Ph, C_2H_3, (CO)NH_2, (CO)OCH_3, Ph, CONSTRUCT \}$ (CO)H, NO₂, C₂H, (CO)CH₃, CN}. The substituents are positioned in the opposite directions to one another. A substituted cobaltocenium is placed within the reference simulation model; the number of environmental water molecules is slightly adjusted to accommodate the increase size of cation for different Y while maintaining the water density of around 15 [1/1000 Å³]. Overall, the number of removed water molecule is 2-3 based on the number of atoms in the substituent group Y. The MD protocol and analysis are the same as followed above. The diffusion coefficients are listed in Table 4. To rationalize the results, we explored correlations of D to 11 properties of the substituted cations listed in Table 5. The properties, chosen based on prior work by some of these authors, 56 include geometric, chemical and electronic features: the cation size, Co to hydroxide oxygen distance, r_{Co-O} , the separation between the centers of mass of the two Cp rings, d_{COM} , the cation dipole moment and polarizability, the minimum/maximum of the electrostatic potential (ESP), the Hirshfeld charge on CpY fragment, the energies of the highest occupied and lowest unoccupied molecular orbitals (HOMO and LUMO, respectively) of the cation, and the bond dissociation energy of the complex into ions, defined as BDE = $E(CoCp_2^+) + E(OH^-)$ -E(CoCp₂+OH⁻). The BDE was computed using the same DFTB method as used for MD. The ESP features were obtained using Spartan 20⁵⁷ at the B3LYP/6-31+G** level within the implicit Polarized Continuum Model (PCM) for water; the default values of the PCM radius (keyword = PCMRAD) are used for all atoms, except Co for which it is set to PCMRAD= 2.0 Å. The remaining properties and the geometry optimization of the cations and their complexes with OH⁻ were computed with Q-Chem,⁵⁸ employing B3LYP density functional paired with the modified basis 6-31G for Co and 6-31G** for all other atoms as described in Ref. ⁵⁶ The analysis is based on

the Pearson correlation coefficients listed in Table 5 and Table S1. The correlations are computed from the data provided in Table S2. The highest correlations are displayed in Fig. 6.

Table 4: The hydroxide diffusion coefficient for the substituted cobaltocenium with one H-atom on each Cp ring replaced by the Y-group.

Y	D_{OH} [Å $^2/\mathrm{ps}$]
$N(CH_3)_2$	0.609 ± 0.054
OCH ₃	0.690 ± 0.075
Ph	0.589 ± 0.063
C_2H_3	0.719 ± 0.063
CH_3	0.773 ± 0.072
Н	0.398 ± 0.058
(CO)NH ₂	0.442 ± 0.050
(CO)OCH ₃	0.485 ± 0.050
(CO)H	0.527 ± 0.050
CN	0.605 ± 0.064
NO_2	0.370 ± 0.033
C_2H	0.607 ± 0.052
(CO)CH ₃	0.456 ± 0.054

As seen in Table 5, out of 11 computed properties, the highest correlations of D_{OH} are to the ESP maximum, LUMO of the cation and the BDE of the complex. The at-first-glance surprising lack of correlation with the dipole moment is understood by considering the cation's structure involving two substituent groups pointing in the opposite directions. This means that even the species with significant charge variation within the molecule may be characterized by the low dipole moment. The effect of the molecular polarizability is likely to be weak due to the aqueous environment. The stronger correlation of -0.6 between D_{OH} and the ESP maximum, the latter indicative of the point charges on the cation surface, is due to the positive surface charges attracting the hydroxyl ions, which reduces their mobility thereby decreasing D_{OH} . The negative correlation -0.7 of D_{OH} to the BDE makes sense as higher BDE values mean that the hydroxide is stronger tethered to the cation and is less mobile. Notably, D_{OH} shows high correlation of 0.66 with the lowest unoccupied molecular orbital (LUMO) energy of the cations and with the BDE: lower LUMO energies 'promotes' stronger attraction of the hydroxide electrons and restricted mobility of OH $^-$. As argued in Ref., 56 the LUMO energy was central feature explaining the stability

Table 5: The Pearson correlation coefficients between the cobaltocenium properties (see text for description) and the hydroxide diffusion coefficient. The properties are defined for the cations unless indicated otherwise.

Property	Correlation
size	0.12
r_{Co-O}	0.30
d_{COM}	0.24
charge on CpY	-0.36
ESP minimum	0.42
ESP maximum	-0.60
dipole moment	0.20
polarizability	0.14
E_{HOMO}	0.55
E_{LUMO}	0.66
BDE	-0.70

of the cobaltocenium-hydroxide complexes (with respect to the Cp-containing fragment separation) substituted with the electron withdrawing groups, with the electron withdrawing/donating character quantified by the Hirshfeld charge on the benzene ring when a substituent was attached. In this work, most of the chosen substituent groups are characterized by the positive Hirshfeld charge, i.e. they are electron-withdrawing rather than electron-donating. This implies that D_{OH} positively correlates with the electron withdrawing (including the hydroxide electrons) property of the substituents.

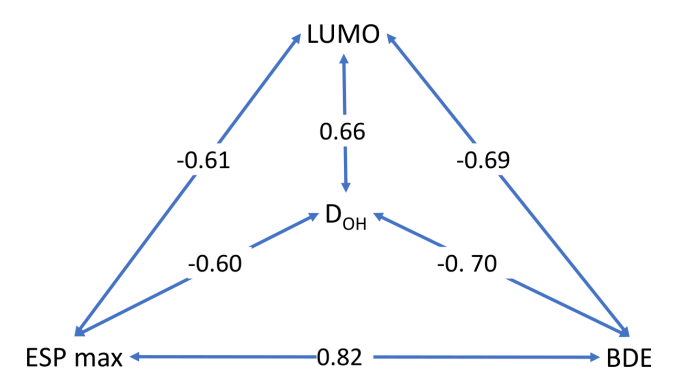


Figure 6: The Pearson correlation coefficients between D_{OH} , the energy of the LUMO and the electrostatic potential (ESP) maximum of the cations, and the ion channel BDE of the cation–OH complex.

3.4 The nuclear quantum effect on the proton hopping

As mentioned in the introduction, the mechanistic details of the structural diffusion in acidic and basic aqueous medium are distinct: the excess proton forms H₃O⁺(H₂O)₃ complex, while the hydroxide ion accepts four H-bonds forming an approximately planar $OH^-(H_2O)_4$ structure. ²¹ In the latter case, the planar OH⁻(H₂O)₄ structure first breaks one H-bond leading to a formation of the tetrahedral $OH^-(H_2O)_3$ complex, followed by the proton hop to the hydroxide. $^{21-23}$ According to the MD results discussed in Section 3.1, under the considered conditions, contribution of the structural diffusion is comparable to that of the vehicular diffusion (Fig. 4). Since the hydrogen-bond network and its rearrangement are essential to the hopping mechanism, the nuclear quantum effects (NQEs) may be significant. ^{22,59–63} Given the size and complexity of the system, we have estimated the NQE on hopping using the following model process described by the potential energy surface (PES). The approach is similar to a recent investigation of the hydrogen transfer meachanism and the associated hydrogen/deuterium isotope effect in Cytochrome P450 Decarboxylase OleT by some of the current authors. ⁶⁴ The hopping proceeds by initially forming H-bond between the transferring H and the hydroxide oxygen; then the covalent bond of the 'donor' H₂O is weakened and the proton moves to the 'acceptor', the hydroxide oxygen. This motion defines the reactive coordinate and the corresponding potential energy curve. Since the minimum energy reactant and product configurations have the same energy, the fully relaxed PES is a symmetric double well, and the hopping is reversible. The changes in the molecular environment, however, may stabilize the proton in the product configuration, and therefore they have to be incorporated into the model. Within a simple model, this is accomplished through the time-dependence of the one-dimensional potential energy curve resulting in an effectively two-dimensional PES, with the time parameterizing the environmental configuration of a segment of the MD simulation during the hopping event. This model captures the dominant features of the environmental motion, which is largely associated with the hydrogen rearrangements; the oxygen atoms are nearly stationary on the time-scale of the proton hop, which is about 100 fs from the MD. However, the model has obvious limitations: it is based on the hopping events identified from the classical MD, and the quantum dynamics is

performed only along the proton transfer coordinate, i.e. there are no quantum corrections to other protonic modes of motion.

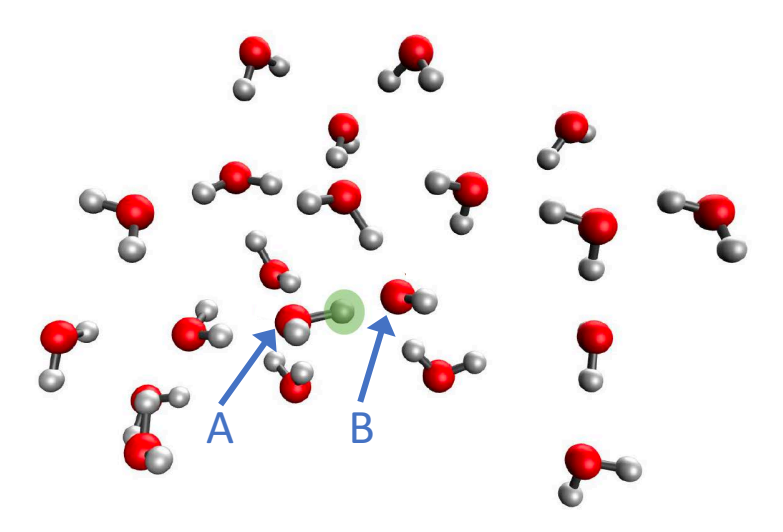


Figure 7: Molecular model used in the PES construction: the water molecules and the hydroxide in the second snapshot (t = 10 fs) where A and B (blue) label the donor and acceptor oxygen atoms (O^A and O^B), respectively, and the hopping proton is highlighted.

To construct the time-dependent PES, we have isolated one of the hopping events for the reference system at water densities of 15.86 [1/1000 ų], which has the highest hydroxide diffusion coefficient. Upon examination of this MD trajectory, we identify a proton transfer unfolding over 120 ps, with the hop occurring around 70 fs of the hopping time interval. Thus, the PES is constructed based on 120 fs of dynamics surrounding the hop. The changing environment was represented by 13 snapshots taken at 10 fs intervals, and the molecular representation was truncated to 20 water molecules as shown in Fig. 7. The potential energy curves were computed for the proton transfer between the donor and acceptor oxygens, labeled O^A and O^B respectively, along the reaction coordinate r, $r := |HO^B| - |HO^A|$. The energy curves are obtained from the partial energy minimization with respect to the positions of the hydrogen atoms attached to the donor and acceptor oxygens while changing the position of hopping proton between donor-acceptor oxygens. The calculations are performed at the B3LYP/6-31+G** level in gas phase using Q-Chem. As time progresses, the PES minimum shifts from positive to negative values of r. For each of the thirteen

system snapshots, the one-dimensional PES scans are computed at 21 points covering the range of $-1.5 \ge r \ge 1.5$ Å and interpolated with the cubic spline fit. At the edges the PES curves are extrapolated with quadratic functions of r. Finally, the cubic spline fit is performed across the one-dimensional curves, in other words along the time-coordinate. The resulting two-dimensional PES of the reaction coordinate and time is shown in Fig. 8(a). The reactant/product sides are described by positive/negative r-values.

To estimate the quantum effects, we compare the reactant well populations obtained from the quantum propagation of the protonic wavefunction and its classical counterpart. The wavefunction is initialized as the Gaussian wave packet,

$$\psi = \left(\frac{2\alpha}{\pi}\right)^{\frac{1}{4}} \exp\left(-\alpha(r-r_0)^2 + \frac{\imath}{\hbar}p_0(r-r_0)\right). \tag{5}$$

The time-dependent Schrödinger equation with the time-dependent PES on ψ is solved on a spatial grid using the split operator/Fast Fourier transform algorithm. The wavefunction time-propagation is performed in atomic units. The initial wavepacket position, r_0 , and width, α , correspond to the vibrational ground state within the local harmonic approximation to the PES at the minimum of the reactant well. The initial momentum p_0 is directed towards the acceptor oxygen, and the corresponding translational energy corresponds to 300 K. The numerical parameter values are $\{\alpha=9.30,\ r_0=-0.784,\ p_0=-1.868\}$ in atomic units (au).

The reactant well (defined as r>0) population as a function of time is shown in Fig. 8(b) alongside the classical result. The latter is based on the dynamics of 2000 classical trajectories, sampling the Wigner distribution corresponding to the initial wavepacket $\psi(r,0)$. At the beginning, both classical and quantum simulations give similar reaction probability. Within 1000 time au, 25% of the reactant goes to the product side; then, however the proton transfer is reversed and at 1500 au, 95% of the probability density is on the reactant side. This behavior correlates with the disappearing and reappearing of the PES reactant well induced by the environment. This oscillatory behavior persists over the following 2000 time au, with the reduced probabilities in the

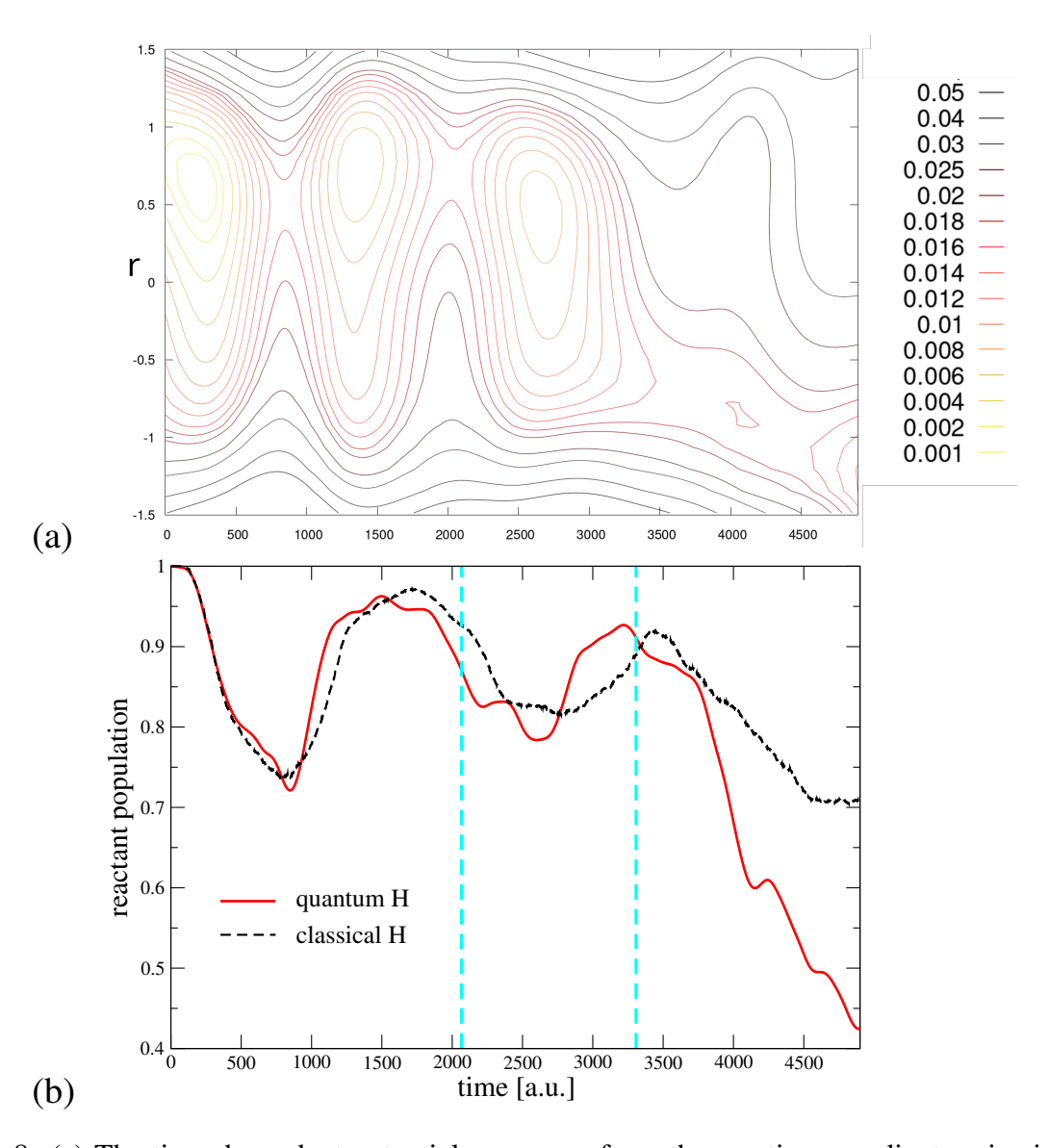


Figure 8: (a) The time-dependent potential energy surface; the reaction coordinate r is given on the vertical axis in Å; the time is given on the horizontal axis in au. The initial wavepacket was centred at $r_0=0.784$ au. (b) The reactant well population as a function of time. The vertical cyan lines mark the interval of the hop in the MD trajectory underlying the developed PES.

reactant well. Within this time, we observed a shallow reactant well that slightly moved toward the product side. After 3500 au, the difference between classical and quantum simulations becomes noticeable. At the end, the quantum nucleus (60% of the probability) rapidly falls into the potential energy well, while only 30% of the classical trajectories end up on the product side. Thus, the ratio of the quantum to classical transfer probability is around 2. Overall, the observed proton transfer dynamics describes an irreversible hop occurring at a particular favorable configuration of the environment, while the quantum/classical difference is attributed to the wavefunction localization.

4 Conclusions

In this work we have analyzed the hydroxide diffusion in the presence of cobaltocenium cations in aqueous environment, based on the the molecular dynamics of model systems confined in one dimension by the graphane sheets to mimic the anion-exchange membrane (AEM) channels. To capture the proton hopping mechanism, we have performed MD computing employing the DFTB electronic structure method. Given the size of the molecular models, comprised of over 500 atoms, the DFTB was chosen to balance the numerical cost with the accuracy. We have analyzed the dependence of the hydroxide diffusion coefficient on the hydration level, arrangement of the cobaltocenium cations and chemical modifications of the cyclopentadienyl rings of the cation, as well as the contribution of the proton hopping underlying the structural diffusion mechanism, and the associated nuclear quantum effects. One limitation of the model comes from the frozen positions of the cation and graphane nuclei during the molecular dynamics, which precludes degradation of the cations and deprotonation of the graphane layers. Other limitations are the classical dynamics of the moving protons (the NQE estimates are based on the nuclear configurations coming from the classical MD), and approximations inherent to DFTB.

Our main findings are: (i) The highest diffusion coefficients of $\sim 0.7\,\text{ Å}^2/\text{ps}$ are achieved at moderate hydration levels corresponding to 60% of the liquid water density; (ii) both the vehicular and structural diffusion mechanisms are important for conductivity with the latter contribut-

ing around 40% at the moderate hydration level and becoming the dominant hydroxide diffusion mechanism at the very low or high hydration levels; (iii) at moderate hydration larger separation between the cations leads to a modest increase in the hydroxide diffusion coefficient, while the orientation of the cations leads to its variability of about 20% on average. We find that at low water densities, neutral water molecules have high diffusion coefficients while for the hydroxyl ions, electrostatically bound to the cobaltocenium cations, those values are relatively low. However, with adequate solvation, the hydroxide diffusion coefficients increase and exhibit maximum values at about half the water density of bulk water. At high water densities a double-layer structure of the water molecules is formed along the membrane walls, effectively reducing the channel size, which greatly impedes the diffusion. The most effective diffusion conditions exist at moderate water densities when there is enough water molecules for solvation, yet enough space for the proton hopping. At these densities, the hydroxyl ion displays the highest diffusion coefficient and both the vehicular and structural diffusion are favored. Despite the unfavorable environment, the proton hopping contributes notably to the diffusion at both low and high densities.

(iv) The effect of the quantum-mechanical nature of the hopping protons was evaluated within a simple, effectively two-dimensional, model. The time-dependent Schrödinger equation has been solved for the protonic wavepacket on a grid in the proton transfer coordinate, using the conventional Split-Operator/Fast Fourier transform approach, with the time-dependence of the potential energy parameterizing the rearrangements of the aqueous environment. The quantum probability of finding the proton in the 'post-hopping' region was found to be 1.7 times higher than the classical one. The effect is attributed to the wavefunction localization, and within this model the hop itself correlates with the shortened distance between the donor and acceptor oxygens and the corresponding hydrogen rearrangement.

Finally, (v) according to the analysis of the hydroxide diffusion with chemically modified cations (a set of 12 cobaltocenium species) the hydroxide diffusion coefficient correlates with the maximum electrostatic potential, dissociation energy of the $Co(Cp)_2^+OH^-$ complex into ions, and the energy of the Lowest Unoccupied Molecular Orbital (LUMO) of the cation. Correlation with

other molecular properties (altogether 11 features were considered within the Pearson correlation analysis) – including the cation dipole moment or polarizability – were found low. Thus, we can state that the cation modifications reducing the positive point charge on its surface or raising its LUMO will increase the anion mobility. These aspects will be further explored theoretically and experimentally in the future.

Supporting Information Available

The Cartesian coordinates of the reference system

Additional diffusion coefficients and cobaltocenium properties

5 Acknowledgment

This material is based upon work supported by the U.S. Department of Energy, Office of Science, Office of Basic Energy Sciences Separation Science program under Award Number DE-SC0020272 and upon work partially supported by the National Science Foundation under Grant No. OIA-1655740, and by a GEAR award (Q.W.) from SC EPSCoR/IDeA Program. Additional support comes from the National Science Foundation CHE-1955768 and CHE-2308922 (S.G.). We acknowledge computational resources of the ACCESS (Advanced Cyberinfrastructure Coordination Ecosystem: Services & Support) program available through allocation TG-DMR110037. This manuscript has been authored in part by UT-Battelle, LLC, under contract DE-AC05-00OR22725 with the US Department of Energy (DOE). The publisher acknowledges the US government license to provide public access under the DOE Public Access Plan (https://energy.gov/doe-publicaccess-plan).

References

- (1) Zhu, T.; Sha, Y.; Yan, J.; Pageni, P.; Rahman, M. A.; Yan, Y.; Tang, C. Metallo-Polyelectrolytes as a Class of Ionic Macromolecules for Functional Materials. *Nat. Commun.* **2018**, *9*, 1–15.
- (2) Shin, D. W.; Guiver, M. D.; Lee, Y. M. Hydrocarbon-Based Polymer Electrolyte Membranes: Importance of Morphology on Ion Transport and Membrane Stability. *Chem. Rev.* **2017**, *117*, 4759–4805.
- (3) Yang, W.; Liu, S.; Yan, J.; Zhong, F.; Jia, N.; Yan, Y.; Zhang, Q. Metallo-Polyelectrolyte-Based Robust Anion Exchange Membranes via Acetalation of a Commodity Polymer. *Macro-molecules* **2021**, *54*, 9145–9154.
- (4) Couture, G.; Alaaeddine, A.; Boschet, F.; Ameduri, B. Polymeric Materials As Anion-Exchange Membranes for Alkaline Fuel Cells. *Prog. Polym. Sci.* **2011**, *36*, 1521–1557.
- (5) Agel, E.; Bouet, J.; Fauvarque, J. Characterization and Use of Anionic Membranes for Alkaline Fuel Cells. *J. Power Sources* **2001**, *101*, 267–274.
- (6) Iojoiu, C.; Chabert, F.; Maréchal, M.; Kissi, N. E.; Guindet, J.; Sanchez, J.-Y. From Polymer Chemistry to Membrane Elaboration: A Global Approach of Fuel Cell Polymeric Electrolytes. *J. Power Sources* 2006, 153, 198–209.
- (7) Zelovich, T.; Vogt-Maranto, L.; Hickner, M. A.; Paddison, S. J.; Bae, C.; Dekel, D. R.; Tuckerman, M. E. Hydroxide Ion Diffusion in Anion-Exchange Membranes at Low Hydration: Insights from Ab Initio Molecular Dynamics. *Chem. Mater.* **2019**, *31*, 5778–5787.
- (8) Lindberg, G. E.; Knight, C.; Felberg, L. E.; Voth, G. A. Molecular Dynamics Simulations of Hydroxide Solvation and Transport in Anionic Exchange Membranes. *ECS Trans* . **2013**, *50*, 2053.

- (9) Chen, C.; Tse, Y.-L. S.; Lindberg, G. E.; Knight, C.; Voth, G. A. Hydroxide Solvation and Transport in Anion Exchange Membranes. *J. Am. Chem. Soc.* **2016**, *138*, 991–1000.
- (10) Zhu, T.; Xu, S.; Rahman, A.; Dogdibegovic, E.; Yang, P.; Pageni, P.; Kabir, M. P.; Zhou, X.-d.; Tang, C. Cationic Metallo-Polyelectrolytes for Robust Alkaline Anion-Exchange Membranes. *Angew. Chem.* 2018, 130, 2412–2416.
- (11) Merinov, B. V.; Goddard III, W. A. Computational Modeling of Structure and OH- Anion Diffusion in Quaternary Ammonium Polysulfone Hydroxide–Polymer Electrolyte for Application in Electrochemical Devices. *J. Membr. Sci.* 2013, 431, 79–85.
- (12) Chen, N.; Long, C.; Li, Y.; Lu, C.; Zhu, H. Ultrastable and High Ion-Conducting Polyelectrolyte Based on Six-Membered N-Spirocyclic Ammonium for Hydroxide Exchange Membrane Fuel Cell Applications. *ACS Appl. Mater. Interfaces* **2018**, *10*, 15720–15732.
- (13) Zhu, T.; Sha, Y.; Firouzjaie, H. A.; Peng, X.; Cha, Y.; Dissanayake, D. M.; Smith, M. D.; Vannucci, A. K.; Mustain, W. E.; Tang, C. Rational Synthesis of Metallo-Cations Toward Redox-and Alkaline-Stable Metallo-Polyelectrolytes. *J. Am. Chem. Soc.* 2019, 142, 1083–1089.
- (14) Zhang, W.; Dong, D.; Bedrov, D.; Van Duin, A. C. Hydroxide Transport and Chemical Degradation in Anion Exchange Membranes: A Combined Reactive and Non-Reactive Molecular Simulation Study. J. Mater. Chem. A 2019, 7, 5442–5452.
- (15) Lindberg, G. E.; Knight, C.; Jorn, R.; Dama, J. F.; Voth, G. A. Multiscale Simulation of Hydroxide Solvation and Transport in Anion Exchange Membranes. *ECS Trans* . **2011**, *41*, 1785.
- (16) Zelovich, T.; Long, Z.; Hickner, M.; Paddison, S. J.; Bae, C.; Tuckerman, M. E. Ab Initio Molecular Dynamics Study of Hydroxide Diffusion Mechanisms in Nanoconfined Structural Mimics of Anion Exchange Membranes. J. Phys. Chem. C 2019, 123, 4638–4653.

- (17) Ren, L.; Hardy, C. G.; Tang, S.; Doxie, D. B.; Hamidi, N.; Tang, C. Preparation of Side-Chain 18-E Cobaltocenium-Containing Acrylate Monomers and Polymers. *Macromolecules* **2010**, 43, 9304–9310.
- (18) Agmon, N. The Grotthuss Mechanism. *Chem. Phys. Lett* **1995**, 244, 456–462.
- (19) Castaneda, S.; Ribadeneira, R. Description of Hydroxide Ion Structural Diffusion in a Quaternized SEBS Anion Exchange Membrane Using Ab Initio Molecular Dynamics. *J. Phys. Chem. C* **2020**, *124*, 9834–9851.
- (20) Hassanali, A.; Giberti, F.; Cuny, J.; Kühne, T. D.; Parrinello, M. Proton Transfer Through the Water Gossamer. *Proc. Natl. Acad. Sci. U.S.A.* **2013**, *110*, 13723–13728.
- (21) Tuckerman, M. E.; Marx, D.; Parrinello, M. The Nature and Transport Mechanism of Hydrated Hydroxide Ions in Aqueous Solution. *Nature* **2002**, *417*, 925–929.
- (22) Marx, D.; Chandra, A.; Tuckerman, M. E. Aqueous Basic Solutions: Hydroxide Solvation, Structural Diffusion, and Comparison to the Hydrated Proton. *Chem. Rev.* **2010**, *110*, 2174–2216.
- (23) Tuckerman, M. E.; Chandra, A.; Marx, D. Structure and Dynamics of OH-(aq). *Acc. Chem. Res.* **2006**, *39*, 151–158.
- (24) Han, K. W.; Ko, K. H.; Abu-Hakmeh, K.; Bae, C.; Sohn, Y. J.; Jang, S. S. Molecular Dynamics Simulation Study of a Polysulfone-Based Anion Exchange Membrane in Comparison with the Proton Exchange Membrane. *J. Phys. Chem. C* **2014**, *118*, 12577–12587.
- (25) Zhang, W.; Van Duin, A. C. ReaxFF Reactive Molecular Dynamics Simulation of Functionalized Poly (phenylene Oxide) Anion Exchange Membrane. *J. Phys. Chem. C* **2015**, *119*, 27727–27736.
- (26) Dubey, V.; Maiti, A.; Daschakraborty, S. Predicting the Solvation Structure and Vehicular

- Diffusion of Hydroxide Ion in an Anion Exchange Membrane Using Nonreactive Molecular Dynamics Simulation. *Chem. Phys. Lett* **2020**, *755*, 137802.
- (27) Dong, D.; Zhang, W.; Van Duin, A. C.; Bedrov, D. Grotthuss Versus Vehicular Transport of Hydroxide in Anion-Exchange Membranes: Insight from Combined Reactive and Nonreactive Molecular Simulations. *J. Phys. Chem. Lett.* **2018**, *9*, 825–829.
- (28) Elstner, M.; Seifert, G. Density Functional Tight Binding. *Philos. Trans. R. Soc. Lond., B, Biol. Sci.* **2014**, *372*, 20120483.
- (29) Gaus, M.; Cui, Q.; Elstner, M. DFTB3: Extension of the Self-Consistent-Charge Density-Functional Tight-Binding Method (SCC-DFTB). *J. Chem. Theor. Comp.* **2011**, *7*, 931–948.
- (30) Zheng, G.; Lundberg, M.; Jakowski, J.; Vreven, T.; Frisch, M. J.; Morokuma, K. Implementation and Benchmark Tests of the DFTB Method and Its Application in the ONIOM Method. *Int. J. Quantum Chem.* **2009**, *109*, 1841–1854.
- (31) Stuart, S. J.; Nugawela, D.; Hadri, B.; Jakowski, J.; Krstic, P.; Garashchuk, S.; Irle, S. Optimization of Density Functional Tight-Binding and Classical Reactive Molecular Dynamics for High-Throughput Simulations of Carbon Materials. Conference Proceedings of XSEDE12. 2012.
- (32) Devanathan, R.; Venkatnathan, A.; Rousseau, R.; Dupuis, M.; Frigato, T.; Gu, W.; Helms, V. Atomistic Simulation of Water Percolation and Proton Hopping in Nafion Fuel Cell Membrane. *J. Phys. Chem. B* **2010**, *114*, 13681–13690.
- (33) Zhang, W.; Van Duin, A. C. Second-Generation ReaxFF Water Force Field: Improvements in the Description of Water Density and OH-Anion Diffusion. *J. Phys. Chem. B* **2017**, *121*, 6021–6032.
- (34) Takaba, H.; Shimizu, N.; Hisabe, T.; Alam, M. K. Modeling of Transport Mechanisms of OH-in Electrolyte of Alkaline Fuel Cell. *ECS Trans* . **2014**, *61*, 63.

- (35) Lee, S. H.; Rasaiah, J. C. Proton Transfer and the Mobilities of the H+ and OH- Ions from Studies of a Dissociating Model for Water. *J. Chem. Phys.* **2011**, *135*, 124505.
- (36) Elstner, M.; Porezag, D.; Jungnickel, G.; Elsner, J.; Haugk, M.; Frauenheim, T.; Suhai, S.; Seifert, G. Self-Consistent-Charge Density-Functional Tight-Binding Method for Simulations of Complex Materials Properties. *Phys. Rev. B* 1998, 58, 7260.
- (37) Oliveira, A. F.; Seifert, G.; Heine, T.; Duarte, H. A. Density-Functional Based Tight-Binding: An Approximate DFT Method. *J. Braz. Chem. Soc.* **2009**, *20*, 1193–1205.
- (38) Nishimura, Y.; Nakai, H. Dcdftbmd: Divide-and-Conquer Density Functional Tight-Binding Program for Huge-System Quantum Mechanical Molecular Dynamics Simulations. *J. Comp. Chem.* **2019**, *40*, 1538–1549.
- (39) Sakti, A. W.; Nishimura, Y.; Nakai, H. Divide-and-Conquer-Type Density-Functional Tight-Binding Simulations of Hydroxide Ion Diffusion in Bulk Water. *J. Phys. Chem. B* **2017**, *121*, 1362–1371.
- (40) Nakai, H.; Sakti, A. W.; Nishimura, Y. Divide-and-Conquer-Type Density-Functional Tight-Binding Molecular Dynamics Simulations of Proton Diffusion in a Bulk Water System. *J. Phys. Chem. B* **2016**, *120*, 217–221.
- (41) Choi, T. H.; Liang, R.; Maupin, C. M.; Voth, G. A. Application of the SCC-DFTB Method to Hydroxide Water Clusters and Aqueous Hydroxide Solutions. *J. Phys. Chem. B* **2013**, *117*, 5165–5179.
- (42) Hourahine, B.; Aradi, B.; Blum, V.; Bonafé, F.; Buccheri, A.; Camacho, C.; Cevallos, C.; Deshaye, M.; Dumitrică, T.; Dominguez, A., et al. DFTB+, a Software Package for Efficient Approximate Density Functional Theory Based Atomistic Simulations. *J. Chem. Phys.* **2020**, *152*, 124101.

- (43) Zheng, G.; Witek, H. A.; Bobadova-Parvanova, P.; Irle, S.; Musaev, D. G.; Prabhakar, R.; Morokuma, K.; Lundberg, M.; Elstner, M.; Köhler, C., et al. Parameter Calibration of Transition-Metal Elements for the Spin-Polarized Self-Consistent-Charge Density-Functional Tight-Binding (DFTB) Method: Sc, Ti, Fe, Co, and Ni. J. Chem. Theor. Comp. 2007, 3, 1349–1367.
- (44) Martyna, G. J.; Tuckerman, M. E.; Tobias, D. J.; Klein, M. L. Explicit Reversible Integrators for Extended Systems Dynamics. *Mol. Phys.* **1996**, *87*, 1117–1157.
- (45) Pranami, G.; Lamm, M. H. Estimating Error in Diffusion Coefficients Derived from Molecular Dynamics Simulations. *J. Chem. Theor. Comp.* **2015**, *11*, 4586–4592.
- (46) Dalton, B. A.; Sbalzarini, I. F.; Hanasaki, I. Fundamentals of the Logarithmic Measure for Revealing Multimodal Diffusion. *Biophys. J.* **2021**, *120*, 829–843.
- (47) Cherstvy, A. G.; Vinod, D.; Aghion, E.; Sokolov, I. M.; Metzler, R. Scaled Geometric Brownian Motion Features Sub- or Superexponential Ensemble-Averaged, but Linear Time-Averaged Mean-Squared Displacements. *Phys. Rev. E* . **2021**, *103*, 062127.
- (48) Wang, B.; Wu, Y.; Liu, D.; Vasenko, A. S.; Casanova, D.; Prezhdo, O. V. Efficient Modeling of Quantum Dynamics of Charge Carriers in Materials Using Short Nonequilibrium Molecular Dynamics. *J. Phys. Chem. Lett.* **0**, 0, 8289–8295, PMID: 37681642.
- (49) Sorte, E. G.; Paren, B. A.; Rodriguez, C. G.; Fujimoto, C.; Poirier, C.; Abbott, L. J.; Lynd, N. A.; Winey, K. I.; Frischknecht, A. L.; Alam, T. M. Impact of Hydration and Sulfonation on the Morphology and Ionic Conductivity of Sulfonated Poly(phenylene) Proton Exchange Membranes. *Macromolecules* 2019, 52, 857–876.
- (50) Dubey, V.; Daschakraborty, S. Translational Jump-Diffusion of Hydroxide Ion in Anion Exchange Membrane: Deciphering the Nature of Vehicular Diffusion. *The Journal of Physical Chemistry B* **2022**, *126*, 2430–2440.

- (51) Zhai, F.-H.; Zhan, Q.-Q.; Yang, Y.-F.; Ye, N.-Y.; Wan, R.-Y.; Wang, J.; Chen, S.; He, R.-H. A Deep Learning Protocol for Analyzing and Predicting Ionic Conductivity of Anion Exchange Membranes. *J. Membr. Sci.* 2022, 642, 119983.
- (52) Dang, H.-S.; Jannasch, P. a Comparative Study of Anion-Exchange Membranes Tethered with Different Hetero-Cycloaliphatic Quaternary Ammonium Hydroxides. *J. Mater. Chem. A* 2017, 5, 21965–21978.
- (53) Wei, C.; Yu, W.; Wu, L.; Ge, X.; Xu, T. Physically and Chemically Stable Anion Exchange Membranes with Hydrogen-Bond Induced Ion Conducting Channels. *Polymers* **2022**, *14*, 4920.
- (54) Chen, N.; Jin, Y.; Liu, H.; Hu, C.; Wu, B.; Xu, S.; Li, H.; Fan, J.; Lee, Y. M. Insight into the Alkaline Stability of N-Heterocyclic Ammonium Groups for Anion-Exchange Polyelectrolytes. *Angew. Chem.* **2021**, *133*, 19421–19429.
- (55) Arges, C. G.; Zhang, L. Anion Exchange Membranes' Evolution Toward High Hydroxide Ion Conductivity and Alkaline Resiliency. *ACS Appl. Energy Mater.* **2018**, *1*, 2991–3012.
- (56) Wetthasinghe, S. T.; Li, C.; Lin, H.; Zhu, T.; Tang, C.; Rassolov, V.; Wang, Q.; Garashchuk, S. Correlation Between the Stability of Substituted Cobaltocenium and Molecular Descriptors.
 J. Phys. Chem. A 2022, 126, 80–87.
- (57) Spartan'20; Computational Chemistry Software; Wavefunction, Inc.: Irvine, CA, 2020.
- (58) Shao, Y.; Gan, Z.; Epifanovsky, E.; Gilbert, A. T. B.; Wormit, M.; Kussmann, J.; Lange, A. W.; Behn, A.; Deng, J.; Feng, X.; *et. al.*, Advances in Molecular Quantum Chemistry Contained in the Q-Chem 4 Program Package. *Mol. Phys.* **2015**, *113*, 184–215.
- (59) Marsalek, O.; Markland, T. E. Quantum Dynamics and Spectroscopy of Ab Initio Liquid Water: The Interplay of Nuclear and Electronic Quantum Effects. J. Phys. Chem. Lett. 2017, 8, 1545–1551.

- (60) Park, K.; Gotz, A. W.; Walker, R. C.; Paesani, F. Application of Adaptive QM/MM Methods to Molecular Dynamics Simulations of Aqueous Systems. *J. Chem. Theor. Comp.* **2012**, 8, 2868–2877.
- (61) Habershon, S.; Markland, T. E.; Manolopoulos, D. E. Competing Quantum Effects in the Dynamics of a Flexible Water Model. *J. Chem. Phys.* **2009**, *131*, 024501.
- (62) Ceriotti, M.; Cuny, J.; Parrinello, M.; Manolopoulos, D. E. Nuclear Quantum Effects and Hydrogen Bond Fluctuations in Water. *Proc. Natl. Acad. Sci. U.S.A.* **2013**, *110*, 15591–15596.
- (63) Spura, T.; John, C.; Habershon, S.; Kühne, T. D. Nuclear Quantum Effects in Liquid Water from Path-Integral Simulations Using an Ab Initio Force-Matching Approach. *Mol. Phys.* 2015, 113, 808–822.
- (64) Dutra, M.; Amaya, J. A.; McElhenney, S.; Manley, O. M.; Makris, T. M.; Rassolov, V.; Garashchuk, S. Experimental and Theoretical Examination of the Kinetic Isotope Effect in Cytochrome P450 Decarboxylase OleT. *J. Phys. Chem. B* 2022, *126*, 3493–3504, PMID: 35508080.
- (65) Kosloff, R. Time-Dependent Quantum-Mechanical Methods for Molecular Dynamics. *J. Phys. Chem.* **1988**, *92*, 2087–2100.
- (66) Feit, M. D.; Fleck Jr., J. A.; Steiger, A. Solution of the Schrödinger Equation by a Spectral Method. *J. Comp. Phys.* **1982**, *47*, 412 433.

Graphical TOC Entry

